
DRAFT CMS Paper

The content of this note is intended for CMS internal use and distribution only

2009/07/23

Archive Id: 1.11

Archive Date: 2009/07/22 19:24:35

Alignment of the CMS Muon System with Cosmic Ray and Beam-Halo Tracks

The CMS Collaboration

Abstract

This paper describes algorithms to align the CMS muon system with tracks and the results of those algorithms using beam-halo muons from the 2008 LHC circulating beam tests and cosmic ray muons from the 2008 Cosmic Run at Four Tesla (CRAFT) exercise. We provide a theoretical description of each algorithm, results of simulations, and cross-checks of the results with real data.

PDFAuthor:	Some Cool Dudes, A. Cern Person
PDFTitle:	Muon Track-based alignment
PDFSubject:	CMS
PDFKeywords:	CMS, detectors, alignment, tracks

Contents

1	1	Introduction and Geometry	1
2	1.1	Geometry of the muon system	1
3	1.2	Coordinate systems and conventions	2
4	2	Local DT Alignment	4
5	2.1	Algorithm for General DT Layer Alignment	4
6	2.2	Independent Cross-Check of δ_z	6
7	3	Local CSC Alignment	8
8	3.1	Overlap Method Algorithm	8
9	3.2	Monte Carlo Study	10
10	3.3	Alignment Results	10
11	4	Global Muon Alignment	12
12	4.1	The HIP Algorithm	12
13	4.2	The MilliPede Algorithm	14
14	4.3	Monte Carlo Study and Discussion of Systematic Errors	16
15	4.4	Global Alignment Results and Cross-Checks	18
16	5	Conclusions	21

1 Introduction and Geometry

The CMS experiment [1] features a large muon tracking system for identifying muons and reconstructing their momenta. As with all tracking systems, the momentum resolution of reconstructed tracks depends both on the intrinsic position resolution of its detector elements and on their alignment. By “alignment,” we mean measurement of the detector elements’ positions and orientations in space, 3 translational plus 3 rotational degrees of freedom, knowledge which allows us to transform hit positions from detector-bound local coordinate systems into a common coordinate system for all CMS tracking systems.

This paper describes methods for aligning barrel Drift Tube (DT) chambers and endcap Cathode Strip Chambers (CSC) and their internal layers with tracks, as well as results of alignments using cosmic rays from the 2008 Cosmic Run at Four Tesla (CRAFT) exercise and beam-halo tracks from the 2008 LHC injection. We will consider two cases: (1) alignment relative to the modular structures from which the muon system is built, and (2) alignment in a single coordinate system defined by the central CMS tracker. Alignment using integrated physical measurement devices such as lasers, rulers, and inclinometers is described elsewhere [2], as are the details of the data transfer and computing model which is used to implement these algorithms [3].

The scale of desired alignment precision is given by the intrinsic resolution of the chambers: 100–300 μm . Since alignment errors and measurement errors add in quadrature, misalignment becomes irrelevant once it is significantly below the intrinsic hit resolution.

1.1 Geometry of the muon system

The muon system is a collection of independent tracking chambers, each of which contains parallel measurement planes, here called chamber layers. The chambers are mounted on 5 moveable barrel wheels (labeled -2 through $+2$) and 6 endcap disks (3 per endcap). Within these large structures, chambers are arranged in stations, labeled in Figure 1, with azimuthal

positions called sectors (in the barrel) or simply chamber number (in the endcap). Barrel stations 1–3 have 12 sectors, station 4 has 14 sectors, and most rings of chambers in the endcap have 36 chambers, the exceptions being ME2/1, ME3/1, and ME4/1, which have 18.

Barrel DT chambers have internal structure: superlayers containing 4 layers each. Stations 1–3 have 3 superlayers, the middle one measuring a direction orthogonal to the outer two. Station 4 chambers have no middle superlayer (only superlayers 1 and 3). Endcap CSCs contain 6 identical layers, each of which measures both coordinates with intersecting cathode strips and anode wires.

1.2 Coordinate systems and conventions

The Alignment Integration Frame, a coordinate system in which all tracking systems are to be aligned, is defined by the tracker. The origin of this system is the center of mass of the tracker's detector elements [4], close to the LHC interaction point, and oriented such that the $+z$ axis points roughly along the beamline, to the west. The $+y$ axis points vertically upward, with $+x$ forming a right-handed coordinate system by pointing south [5]. These same coordinates can be expressed cylindrically, with x and y replaced by $r = \sqrt{x^2 + y^2}$ and $\phi = \tan^{-1}(y/x)$. The curvilinear coordinate $r\phi$ is perpendicular to the beamline and to rays from the beamline, and differentials of $r\phi$ are understood to vary in ϕ , not r (so $d(r\phi)$ is equivalent to $r d\phi$).

Each muon chamber and layer has its own local coordinate system, centered on the subdetector with local z being perpendicular to the measurement planes, and $+z$ points in the direction of decreasing layer number. The local x axis roughly corresponds to global $r\phi$ (though for some chambers the direction is reversed), and local y forms a right-handed coordinate system. In the absence of misalignment, y is parallel to the beamline for DT chambers and radial for CSCs.

Layer/superlayer coordinate systems differ slightly from their parent chambers. The origin of each coordinate system is centered such that $z = 0$ lies on the layer and the average of layers in the superlayer, and both layers and superlayers have small offsets in x as well. The middle superlayer of DT chambers (superlayer 2) are rotated by 90° with respect to the chamber coordinates, such that x measurements in these layers are y positions in chamber coordinates. Internal alignments of layers introduce additional corrections.

Cathode strips in CSC layers fan radially from the beamline, intersected by anode wires. The strips measure a coordinate perpendicular to their orientation, which in the absence of misalignment coincides with global $r\phi$ throughout the chamber. We find “local $r\phi$,” or local x times the cosine of the strip angle, to be a more convenient coordinate than x for CSCs. This is because local $r\phi$ is determined purely by high-precision strip measurements, avoiding input from the groups of ganged wires which would introduce a complicated and large-scale (cm) granularity to the residuals distributions.

We describe the orientations of chambers and layers with ϕ_x , ϕ_y , and ϕ_z , where each is a right-hand rotation around the corresponding coordinate axis. The 3-D rotation is the following composition:

$$\begin{pmatrix} 1 & 0 & 0 \\ 0 & \cos \phi_x & \sin \phi_x \\ 0 & -\sin \phi_x & \cos \phi_x \end{pmatrix} \cdot \begin{pmatrix} \cos \phi_y & 0 & -\sin \phi_y \\ 0 & 1 & 0 \\ \sin \phi_y & 0 & \cos \phi_y \end{pmatrix} \cdot \begin{pmatrix} \cos \phi_z & \sin \phi_z & 0 \\ -\sin \phi_z & \cos \phi_z & 0 \\ 0 & 0 & 1 \end{pmatrix}. \quad (1)$$

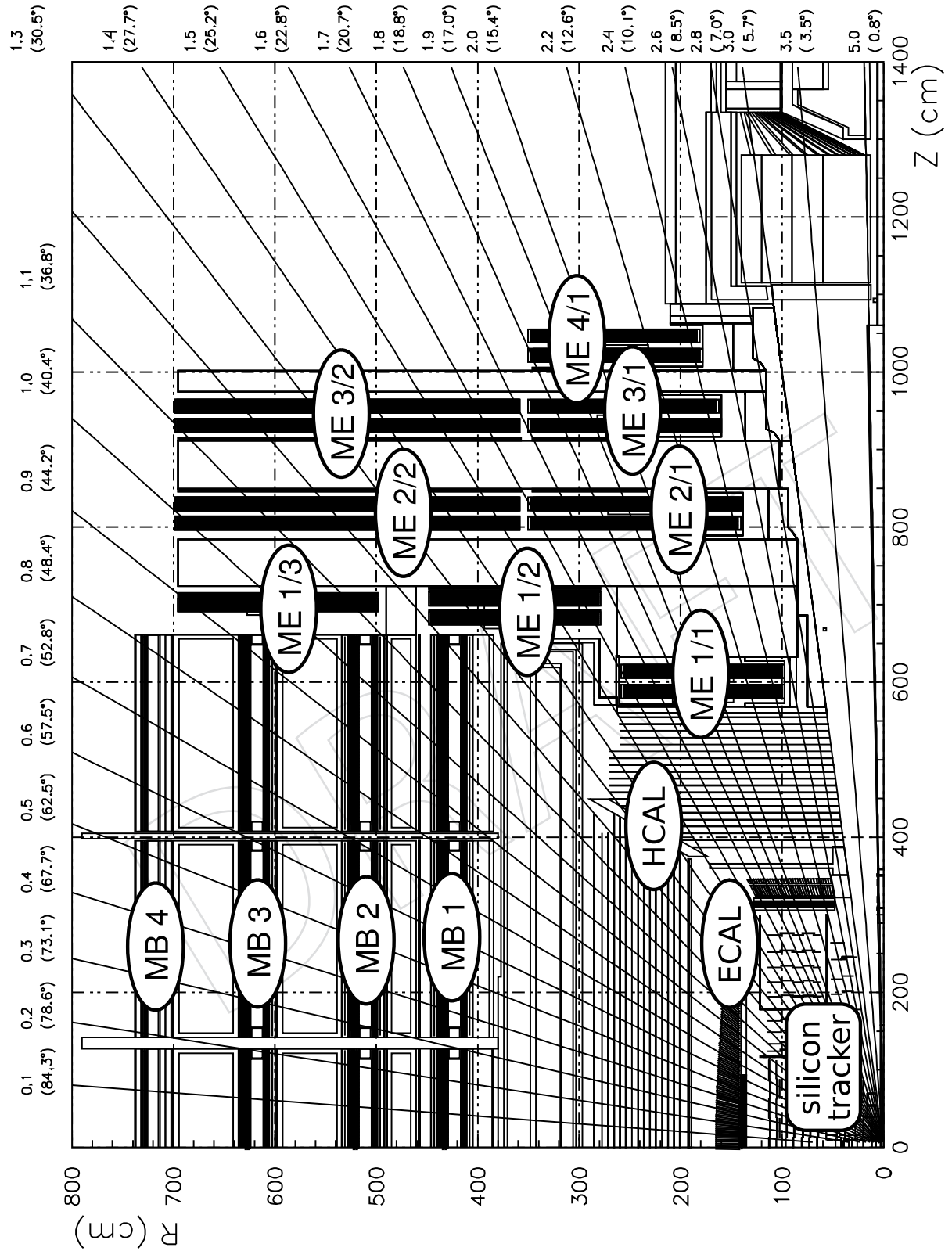


Figure 1: A quarter-view of CMS with labeled muon barrel (MB) and endcap (ME) stations.

2 Local DT Alignment

This section describes the alignment of layers and superlayers within DT chambers, using local information only. Tracking data are combined with physical measurements performed when the chambers were constructed to resolve ambiguities between alignment and track-fitting. The chamber geometry obtained by these methods is an important part of the global alignment described in a later section.

2.1 Algorithm for General DT Layer Alignment

The tracks and physical survey data were merged into a consistent geometry with a method based on the Millepede algorithm of V. Blobel [6]. The basic idea behind this algorithm is to define a χ^2 with contributions from all sources: alignment, track residuals, and survey residuals, and then minimize the χ^2 , allowing all parameters to float.

Alignment corrections are represented by a vector with 6 parameters per alignable (layers, superlayers, and in a later section, the chambers themselves). These are $\delta_x^i, \delta_y^i, \delta_z^i, \delta_{\phi_x}^i, \delta_{\phi_y}^i$, and $\delta_{\phi_z}^i$ with i indexing the alignables. Varying the alignment affects residuals, the difference between experimental hits and fitted track points. Layers and superlayers measure hit positions in only one dimension, so the effect of geometric corrections on residuals ($\Delta x_j^i \text{ geom}$ on alignable i and track j) can be related to alignment parameters through the following matrix:

$$\begin{pmatrix} \Delta x_j^i \text{ geom} \end{pmatrix} = \begin{pmatrix} -1 & 0 & \frac{dx}{dz} & -y \frac{dx}{dz} & x \frac{dx}{dz} & -y \end{pmatrix} \cdot \begin{pmatrix} \delta_x^i \\ \delta_y^i \\ \delta_z^i \\ \delta_{\phi_x}^i \\ \delta_{\phi_y}^i \\ \delta_{\phi_z}^i \end{pmatrix} \quad (2)$$

for each alignable (where y and $\frac{dx}{dz}$ are the track's y position and x slope with respect to z , in the layer's coordinate system). Tracks are most sensitive to δ_x , and they have no sensitivity to δ_y because the term connecting it to Δx^{geom} is zero. We will henceforth denote the vector of all alignment parameters as $\vec{\delta}$, and the matrix connecting them to Δx^{geom} as A (the index i is internal). Expanding equation 2 to cover all alignables,

$$\begin{pmatrix} \Delta x_j^{\text{geom}} \end{pmatrix} = A \cdot \vec{\delta}. \quad (3)$$

Track-fitting is part of the global minimization, so we must include a term corresponding to variation the track parameters. We parameterize tracks inside of DT chambers as straight lines ($x_0, y_0, \frac{dx}{dz}$ and $\frac{dy}{dz}$), since magnetic field lines mainly follow the yokes between chambers, leaving negligible magnetic field in the chambers themselves. The effect of small corrections in the track parameters on residuals $\Delta x_j^{\text{track}}$ is also linear, and may be represented by a matrix multiplying the track parameter corrections

$$\begin{pmatrix} \Delta x_j^{\text{track}} \\ \Delta y_j^{\text{track}} \end{pmatrix} = \begin{pmatrix} 1 & 0 & z_i & 0 \\ 0 & 1 & 0 & z_i \end{pmatrix} \cdot \begin{pmatrix} \delta_{x_0 j} \\ \delta_{y_0 j} \\ \delta_{\frac{dx}{dz} j} \\ \delta_{\frac{dy}{dz} j} \end{pmatrix} \quad (4)$$

in the chamber's coordinate system. (As a reminder, one-dimensional x positions in layer coordinates transform to $(0, x)$ in two-dimensional chamber coordinates for superlayer 2 and

($x, 0$) for superlayers 1 and 3, in the absence of alignment corrections.) We will denote the corrections to the track parameters as $\delta \vec{p}_j$ and the matrix connecting them to x^{track} as B_j , such that Equation 4 becomes

$$\begin{pmatrix} \Delta x_j^{\text{track}} \\ \Delta y_j^{\text{track}} \end{pmatrix} = B_j \cdot \delta \vec{p}_j. \quad (5)$$

The observed residuals $\Delta \vec{x}$ are

$$\Delta \vec{x} = \Delta \vec{x}^{\text{geom}} + \Delta \vec{x}^{\text{track}} + \Delta \vec{x}^{\text{meas}} \quad (6)$$

where $\Delta \vec{x}^{\text{meas}}$ is a random contribution from measurement error, assumed to be symmetric. We can now construct a χ^2 which is minimized when tracks and chamber geometry are mutually consistent:

$$\chi^2_{\text{track-based}} = \sum_j \left(\Delta \vec{x} - A \cdot \vec{\delta} - B_j \cdot \delta \vec{p}_j \right)^T \left(\sigma_{\text{resid}_i}^2 \right)^{-1} \left(\Delta \vec{x} - A \cdot \vec{\delta} - B_j \cdot \delta \vec{p}_j \right) \quad (7)$$

where $\sigma_{\text{resid}_i}^2$ is the covariance matrix of hits (no uncertainty in our track model). However, $\chi^2_{\text{track-based}}$ cannot be minimized: the system has more degrees of freedom than constraints. Consider, for instance, shearing all layers linearly in x ; this non-rigid deformation of the chamber leaves $\chi^2_{\text{track-based}}$ invariant because fitted tracks compensate with $\frac{dx}{dz}$. We therefore must augment it with external data to yield a meaningful alignment.

2.1.1 Quality Control Measurements

As the DT chambers were being built, the positions of the wire end-pins were measured and recorded [7]. Local δ_x^i corrections can be determined from an average of the measurements over layers. Typical (RMS) corrections are 100 μm , with an uncertainty of 30–40 μm . These measurements only constrain the relative positions of layers within each superlayer, not the superlayers relative to one another, because each superlayer was built separately.

2.1.2 Photogrammetry Measurements

After superlayers were assembled into chambers, the position and orientation of the superlayers were measured by photogrammetry (a photograph of reflective targets at known points on the superlayer, in a coordinate system defined by references at their corners [8]). These measurements constrain superlayers relative to one another, but not the layers inside).

Typical corrections are 200 μm for δ_x and δ_y , with 150 μrad for rotations. The δ_z corrections were 1–1.5 mm because of a layer of glue not included in the design description. We take special care to cross-check these δ_z parameters independently with tracks before applying the correction.

2.1.3 Combination

To include survey measurements into the global alignment fit, we need a term to describe the effect of alignment corrections $\vec{\delta}^i$ on the positions of the survey's control points (nominally at x_k, y_k, z_k). This term is

$$\Delta x_k^{\text{points}} = \begin{pmatrix} 1 & 0 & 0 & y_k & z_k & 0 \\ 0 & 1 & 0 & -x_k & 0 & z_k \\ 0 & 0 & 1 & 0 & -x_k & -y_k \end{pmatrix} \cdot \vec{\delta}^i \quad (8)$$

and we denote the matrix for all control points on all alignables as C (alignable index i and survey point index k are internal). This matrix is constructed in such a way as to internally account for the fact that some measurements are relative differences, rather than absolute coordinates. The χ^2 of survey measurements is

$$\chi^2_{\text{survey}} = \left(\Delta \vec{x}^{\text{survey}} - C \cdot \vec{\delta} \right)^T (\sigma_{\text{survey}}^2)^{-1} \left(\Delta \vec{x}^{\text{survey}} - C \cdot \vec{\delta} \right) \quad (9)$$

where $\Delta \vec{x}^{\text{survey}}$ are the measured positions from survey and photogrammetry, and σ_{survey}^2 is their covariance matrix.

Finally, the global chamber position can never be determined from local information, so translations and rotations of the whole chamber are fixed to zero with Lagrange multipliers $f(\lambda)$. The final χ^2 is

$$\chi^2 = \chi^2_{\text{track-based}} + \chi^2_{\text{survey}} + f(\lambda), \quad (10)$$

which we minimize by a straight-forward numerical inversion of the derivatives matrix, as the number of alignable parameters is not large.

2.2 Independent Cross-Check of δ_z

As explained above, the largest correction from the design geometry was in the superlayers' z coordinates, due to a layer of glue not included in the design description. To cross-check these photogrammetry measurements, we determined them from an independent track-based measurement.

As the displacement under study is between superlayers, track segments fitted in each superlayer individually are not affected by the correction. We can therefore simplify the χ^2 by re-defining residuals in this case as a difference between single-superlayer track segments (superlayers 1 and 3 only), extrapolated to a common plane. The B_j matrix vanishes, leaving us with

$$\chi^2 = \sum_j \left(\Delta \vec{x} - A \cdot \vec{\delta} \right)^T (\sigma_{\text{resid}}^2)^{-1} \left(\Delta \vec{x} - A \cdot \vec{\delta} \right) \quad (11)$$

where σ_{resid}^2 is the covariance matrix for these new residuals. We further simplify the alignment by only allowing δ_x , δ_z , and δ_{ϕ_y} to float, as these are the parameters that can be determined purely from track segments in one-dimensional measurement devices. The alignment derivatives matrix A for each chamber is reduced to

$$\left(\Delta x_j^{\text{geom}} \right) = \begin{pmatrix} -1 & \frac{dx}{dz} & x \frac{dx}{dz} \end{pmatrix} \cdot \begin{pmatrix} \delta_x^i \\ \delta_z^i \\ \delta_{\phi_y}^i \end{pmatrix}. \quad (12)$$

A geometric interpretation of the δ_z term is given in Figure 2. With these simplifications, it is possible to align superlayers purely with track-based data.

The δ_z corrections from survey (photogrammetry), this track-based method, and their differences are plotted in Figure 3, revealing independent agreement in non-negligible corrections. Typical discrepancies are $580 \mu\text{m}$ (RMS and Gaussian width) in δ_z , while the size of the corrections range from 1 to 2 mm (thicker glue was used in station 1). The δ_x and δ_{ϕ_y} corrections were also in agreement, but they were negligible ($80 \mu\text{m}$ and $50 \mu\text{rad}$, respectively).

The internal DT geometry used in the global alignment was determined by the combined fit described in subsection 2.1 with δ_z fixed, followed by corrections from the tracks-only method described above. It therefore incorporates all available information except that which is reserved for cross-checking the sources.

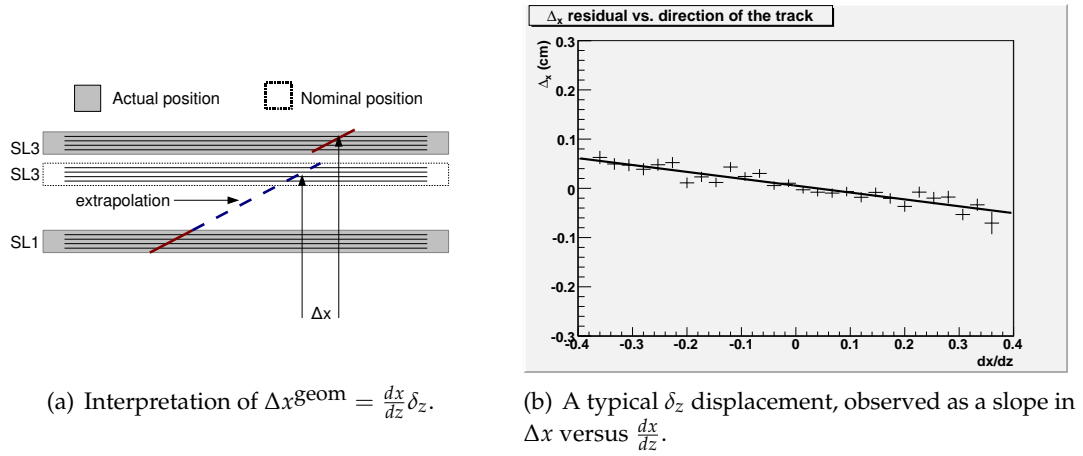
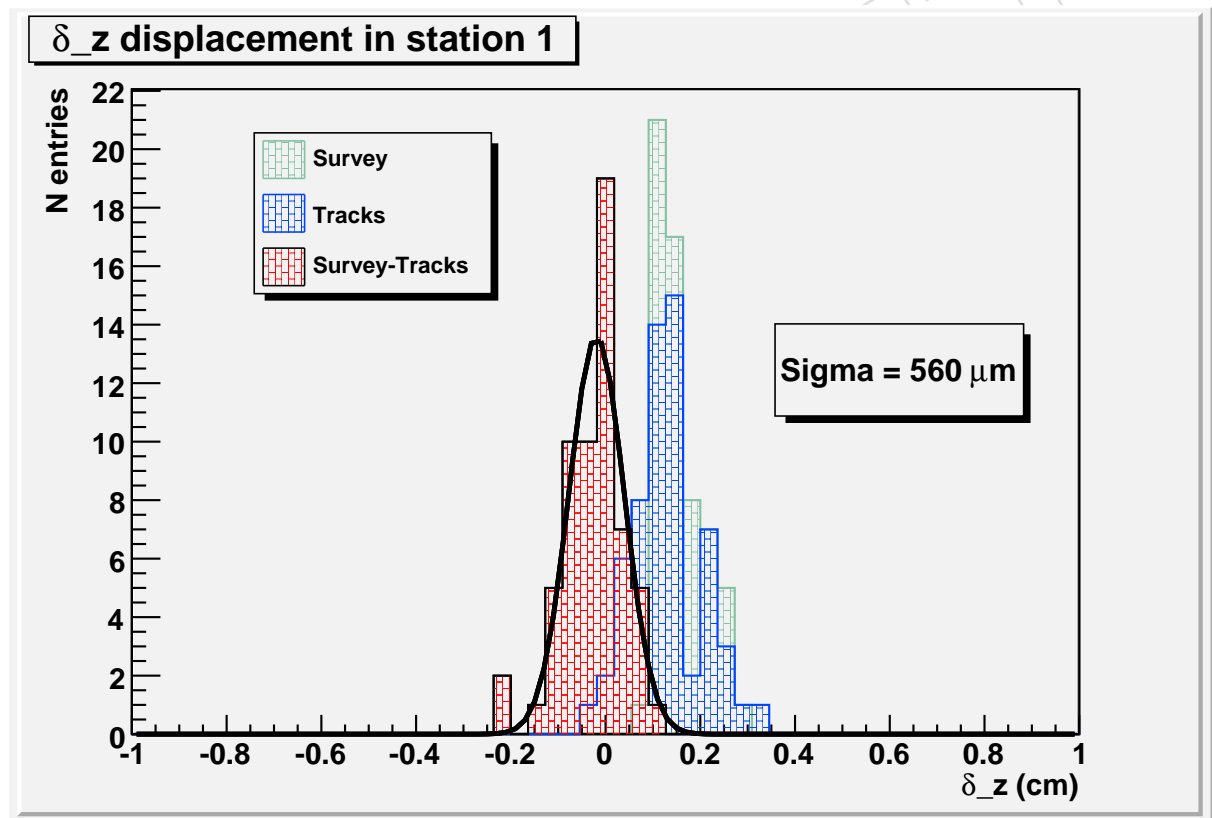
Figure 2: Measuring δ_z with tracks only.

Figure 3: Comparison of survey and track-based alignment of δ_z of superlayers in DT chambers. Each entry in this histogram is a δ_z measurement for one chamber, with the three distributions corresponding to survey (photogrammetry) only, tracks only, and the chamber-by-chamber difference between survey and tracks.

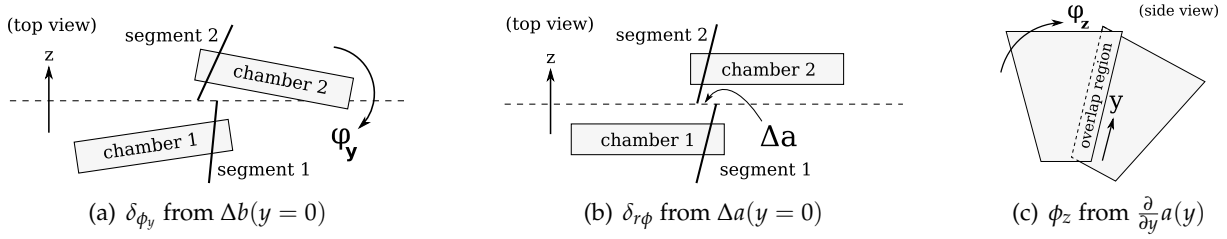


Figure 4: How three track parameters are determined from linear fits to $\Delta a(y)$ and $\Delta b(y)$, where Δa and Δb are the positions and slopes of track segments at a plane between the two CSCs.

3 Local CSC Alignment

The CSCs in the muon endcap were designed to overlap slightly along their edges, such that a track passing through the narrow “overlap regions” would be observed by both of the neighboring chambers, without scattering volumes in between or propagation over large distances. These tracks can therefore measure the relative alignment of the pairs of chambers they connect with high precision. All endcap rings except for ME1/3 are connected in this way by overlaps. In this section, we will describe a method to align CSCs within each ring with only a small sample of tracks and demonstrate the accuracy of the method by comparing its results with an independent measurement.

3.1 Overlap Method Algorithm

The basic strategy is to measure differences in alignment parameters for pairs of chambers and then propagate alignment corrections azimuthally around the ring by solving a system of equations. Relative alignment corrections between overlapping neighboring chambers i and $i+1$ are derived from the consistency of track segments with a single, straight line.

At each interface between two overlapping chambers, we fit hits in the 6 layers of each chamber to straight lines $r\phi_i(z) = a_i + b_i z$ and $r\phi_{i+1}(z) = a_{i+1} + b_{i+1} z$ in a shared coordinate system and then propagate these segments to a plane equidistant between the two chambers (at $z = 0$). The position-matching residual on the plane is $\Delta a = a_i - a_{i+1}$ and the angle-matching residual is $\Delta b = b_i - b_{i+1}$. The overlap region is a thin strip spanning the chamber only along the y dimension, so we can consider fitting these residuals as a function of the track’s y intersection with the plane of comparison (a linear fit of linear track-fits). We therefore have access to four types of residuals:

- $\Delta a(y=0)$: the relative $\delta_{r\phi}$ correction in position along a circle centered on the beam-line,
- $\Delta b(y=0)$: the relative δ_{ϕ_y} angle between the two chambers,
- $\frac{\partial}{\partial y} \Delta a(y)$: the relative δ_{ϕ_z} angle,
- $\frac{\partial}{\partial y} \Delta b(y)$: a non-rigid twist of the chambers.

We consider only the three alignment corrections ($\delta_{r\phi}$, δ_{ϕ_y} , and δ_{ϕ_z}), presented graphically in Figure 4.

While it is possible to resolve all three corrections at once, note that δ_{ϕ_y} is independent of the other two and $\delta_{r\phi}$ is independent of δ_{ϕ_z} . We can therefore ignore dependencies if we align the parameters in the following order: δ_{ϕ_y} , then $\delta_{r\phi}$, and then δ_{ϕ_z} .

The problem of propagating alignment corrections around the ring is identical for each of the

three parameters, so we will present it only once in an abstract way. Label the mean of each residuals distribution $\alpha_{i,i+1}$ (for each of the three types of residuals under consideration) with A_i and A_{i+1} being the alignment corrections for the neighboring chambers (δ_{ϕ_y} , $\delta_{r\phi}$, or δ_{ϕ_z}). Each ring has $N = 18$ or 36 chambers, so i ranges from 1 to N with the convention that $N + 1 = 1$ (to close the loop).

If we move chamber i and $i + 1$ by A_i and A_{i+1} , the mean of the residuals between them can be expected to change by $(A_i - A_{i+1})$. To optimize all of the residuals at once, we define a χ^2 as

$$\chi^2 = (\alpha_{12} - A_1 + A_2)^2 + (\alpha_{23} - A_2 + A_3)^2 + \dots + (\alpha_{N1} - A_N + A_1)^2 \quad (13)$$

and minimize it by setting its derivatives to zero. For example,

$$\frac{1}{2} \frac{\partial \chi^2}{\partial A_2} = (\alpha_{12} - A_1 + A_2) - (\alpha_{23} - A_2 + A_3) = 0. \quad (14)$$

A complete set of such equations, written in matrix form, looks like the following:

$$\begin{pmatrix} \alpha_{1,2} - \alpha_{N,1} \\ \alpha_{2,3} - \alpha_{1,2} \\ \vdots \\ \alpha_{(N-1),N} - \alpha_{(N-2),(N-1)} \\ \alpha_{N,1} - \alpha_{(N-1),N} \end{pmatrix} = \begin{pmatrix} 2 & -1 & & -1 \\ -1 & 2 & -1 & \\ & & \ddots & \\ & & -1 & 2 & -1 \\ -1 & & & -1 & 2 \end{pmatrix} \begin{pmatrix} A_1 \\ A_2 \\ \vdots \\ A_{N-1} \\ A_N \end{pmatrix}. \quad (15)$$

To align all N chambers, we need only invert this $N \times N$ matrix, and N is small enough to be manageable.

Unfortunately, the matrix in Equation 15 is singular because a relative alignment procedure cannot determine the global position of the whole system. Rotating the whole ring rigidly by adding the same constant to every A_i would leave the χ^2 invariant. This is a flat direction in (A_1, A_2, \dots, A_N) space, and it can be unflattened by preferring the corrections A_i to be as small as possible. We add the average of A_i

$$\left[\frac{1}{N} (A_1 + A_2 + \dots + A_N) \right]^2 \quad (16)$$

to the χ^2 so that it will be minimized, and each derivative equation becomes

$$\frac{1}{2} \frac{\partial \chi^2}{\partial A_i} = (\alpha_{i-1,i} - A_{i-1} + A_i) - (\alpha_{i,i+1} - A_i + A_{i+1}) + \frac{1}{N^2} \sum_{i=1}^N A_i = 0. \quad (17)$$

The right-hand-side of Equation 15 becomes

$$\left[\begin{pmatrix} 2 & -1 & & -1 \\ -1 & 2 & -1 & \\ & & \ddots & \\ & & -1 & 2 & -1 \\ -1 & & & -1 & 2 \end{pmatrix} + \frac{1}{N^2} \begin{pmatrix} 1 & 1 & \dots & 1 \\ 1 & 1 & & \\ \vdots & & \ddots & \\ 1 & & & 1 \end{pmatrix} \right] \begin{pmatrix} A_1 \\ A_2 \\ \vdots \\ A_4 \\ A_5 \end{pmatrix}. \quad (18)$$

It has a unique solution in which the average of A_i is exactly zero.

The circular ring of chambers also provides an internal cross-check: the closure

$$\sum_{i=1}^N \alpha_{i,i+1} - (A_i - A_{i+1}) = \sum_{i=1}^N \alpha_{i,i+1} \quad (19)$$

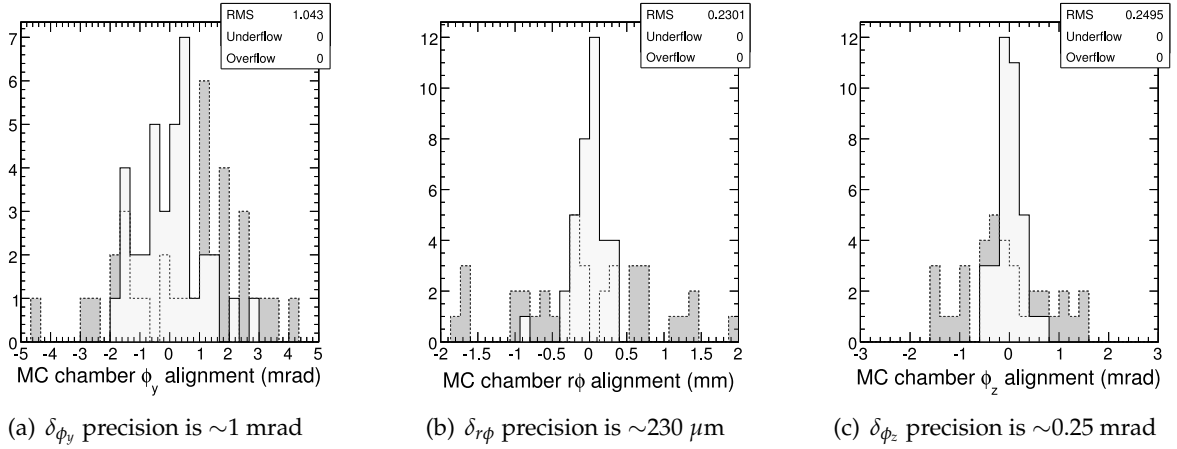


Figure 5: Comparison of CSC alignment parameters with their true values before (dark) and after (light) a simulated beam-halo alignment with similar statistics to the 2008 LHC run.

must be zero. The closure is independent of alignment, because all A_i terms cancel in the sum. A non-zero closure would indicate an incorrect circumference for the ring, either from our description of the chamber widths or their radial distance from the beamline. All measured values of closure were consistent with zero.

This algorithm can be extended to align layers within the CSC chambers, taking advantage of the two-chamber overlap to resolve ambiguities between track-fitting and layer alignment in an isolated chamber. In the 2008 LHC beam-halo run, many layer measurements were not statistically significant, with a precision of $50\text{--}100 \mu\text{m}$, so we do not present the results here.

3.2 Monte Carlo Study

The procedure was first applied to simulated beam-halo with approximately the same number of events as the 2008 LHC run. The azimuthal and radial distributions are not exactly the same as in data, as they are notoriously difficult to predict for a new accelerator. Starting from a misaligned detector, the procedure re-aligned δ_{ϕ_y} with about 1 mrad precision, $\delta_{r\phi}$ with about $230 \mu\text{m}$, and δ_{ϕ_z} with about 0.25 mrad, by comparison with the true positions of the chambers, known in simulation. Figure 5 shows histograms of the differences between aligned values of the parameters and their true values.

3.3 Alignment Results

In September of 2008, protons circulated in beam-2 of the LHC tunnel for 9 minutes, and enough data were collected to test the CSC Overlaps procedure. More beam-halo muons illuminated the inner rings (ring 1) of the minus side of the endcap because beam-halo muons tend to be close to the beamline and beam-2 passed through CMS in the direction from $-z$ toward $+z$. At that time, all chambers in ME-2/1 and ME-3/1 were operational, so we aligned them with the CSC Overlaps algorithm.

To verify the aligned positions, we compare them with photogrammetry measurements. Each chamber has two reflective alignment targets whose positions can be measured with $300 \mu\text{m}$ precision by photographing them in a strong light. From these, $\delta_{r\phi}$ and δ_{ϕ_z} corrections (relative to the design geometry) can be computed with $(300 \mu\text{m})/\sqrt{2} = 210 \mu\text{m}$ and $(300 \mu\text{m}) \cdot \sqrt{2}/\ell = 0.23$ mrad precision, respectively (where ℓ is half the distance between photogrammetry targets, about 1.9 m in this case). Errors from ϕ_y misalignments are negligible in these transfor-

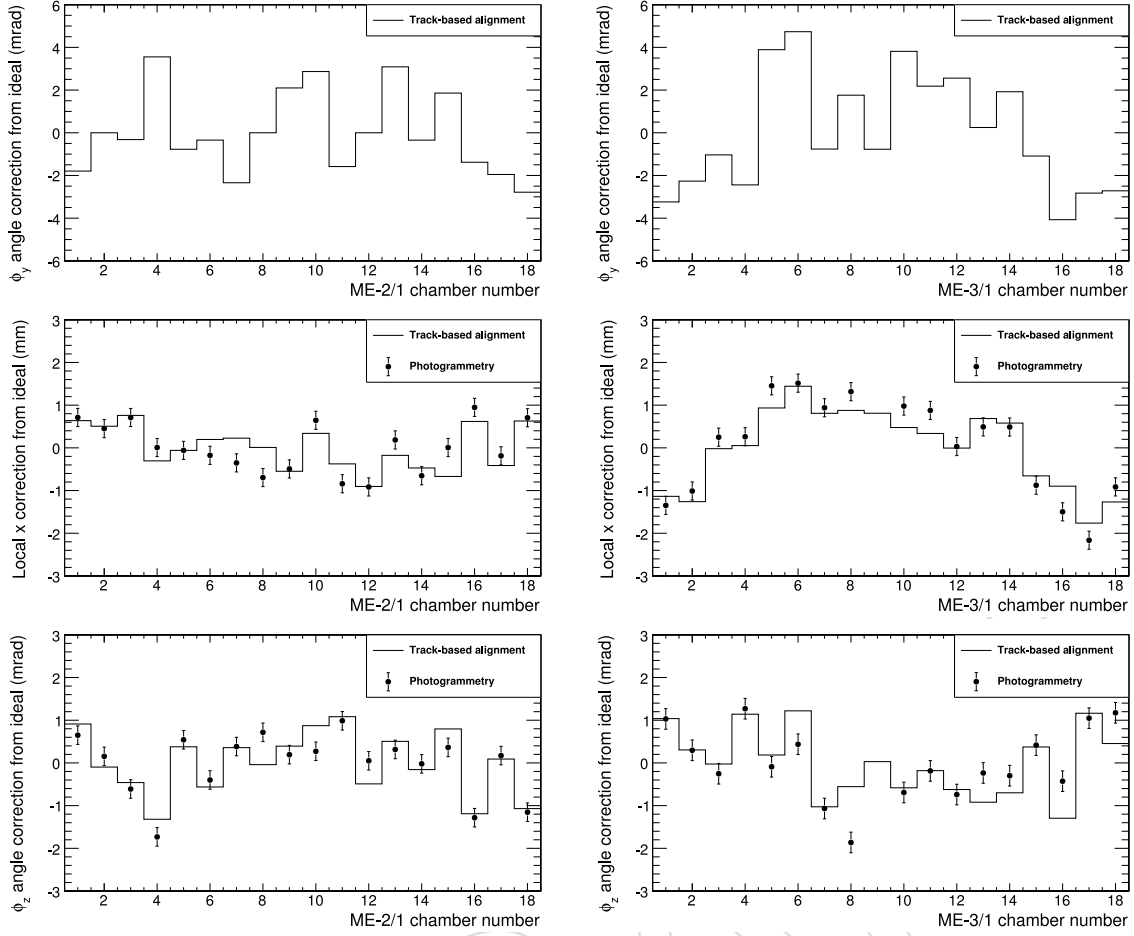


Figure 6: CSC alignment results from the Overlaps procedure and the 2008 LHC run, presented as a difference from ideal and compared with photogrammetry where possible.

mations. The photogrammetry and track-based measurements were both taken with the CMS solenoid turned off. (The solenoid's field is strong enough to move the chambers, invalidating the measurement.) Unlike photogrammetry, the track-based measurement can also be performed with the solenoid on, though no such data were taken while LHC beam-halo muons could be collected.

In Figure 6, the track-based and photogrammetry corrections to ideal geometry are presented. Both yield significant deviations from zero, yet agree rather well. We plot the same data as histograms of differences between track-based and photogrammetry measurements in Figure 7, and observe that the widths of these distributions are $340 \mu\text{m}$ and 0.42 mrad . Subtracting the photogrammetry uncertainties in quadrature from standard deviations observed in the plots,

$$\text{track-based } \delta_{r\phi} \text{ accuracy} = \sqrt{(340 \mu\text{m})^2 - (210 \mu\text{m})^2} = 270 \mu\text{m} \quad (20)$$

$$\text{track-based } \phi_z \text{ accuracy} = \sqrt{(0.42 \text{ mrad})^2 - (0.23 \text{ mrad})^2} = 0.35 \text{ mrad}, \quad (21)$$

in rough agreement with the simulation's prediction and close to the scale of the intrinsic hit resolution of the detectors ($116 \mu\text{m}$). Assuming that the errors are statistical, an hour or more of similar tracks would yield an alignment that is more precise than the intrinsic hit resolution.

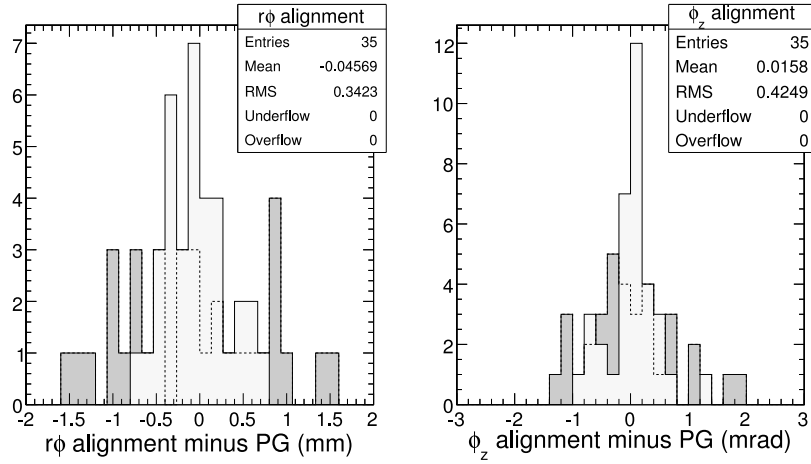


Figure 7: Chamber-by-chamber verification of the beam-halo alignment with photogrammetry. The dark histogram is before alignment; the light histogram and statistics box are after alignment.

4 Global Muon Alignment

Local muon alignment procedures arrange sets of chambers in self-consistent coordinate systems, but cannot relate those coordinates to the locations of other subsystems of CMS, particularly the tracker. In this section, we describe methods to align muon chambers relative to the tracker, such that all tracking volumes in CMS share one global system of coordinates. Since these global alignment methods are partly independent of the local alignments, they can be used to cross-check each other.

Two algorithms, HIP (Hits and Impact Points) and Millepede, have been developed to align muon chambers relative to the tracker. Each is described in its own section below, followed by studies in Monte Carlo simulations, and then results of each with cosmic ray data.

4.1 The HIP Algorithm

The basic idea of the HIP algorithm as it is applied to the muon system is to fit alignables in a “target” tracking volume relative to a well-aligned “reference” volume, usually the silicon tracker. Muon tracks are fitted using information from the reference volume only, and chambers in the target are translated and rotated to minimize the distance between muon hits and the impact points (intersections) of tracks on the layer planes. This differs from the conventional HIP approach [9], which iteratively aligns elements and fits tracks in a single tracking volume.

Thick (20–60 cm) layers of iron are placed between each muon station as a return yoke for the CMS solenoid. In the iron, magnetic fields are stronger than in the gas volume of the chambers, and probabilities are higher that the muon’s trajectory will scatter, making its direction less predictable between chambers than within chambers. To account for this correlation, we combine residuals such that we obtain one independent measurement per chamber per track. This measurement has four components, Δx , Δy , $\Delta \frac{dx}{dz}$, and $\Delta \frac{dy}{dz}$, which are the differences between the propagated track’s two-dimensional location and entrance angle, respectively, with the pattern of hits in the chamber. We compute these four observables from a fit of the residuals versus local z to a straight line. The reduced χ^2 of the linear fit expresses the quality of the measurement (independent of the distance between the track and the hits), so we use N_{dof}/χ^2

as a weight in the final alignment. Station 4 DT chambers can only measure one dimension, so they observe only Δx and $\Delta \frac{dx}{dz}$, and strip measurements in CSCs observe $\Delta r\phi$ and $\Delta d(r\phi)/dz$.

The measurements described above are influenced by four categories of effects:

- misalignment of the target chamber (geometric residuals),
- statistical uncertainty in the track fit,
- propagation errors from large-angle scattering (distributes residuals according to a power law) and the result of many small-angle scattering events (Gaussian “multiple scattering”),
- biases in the track source or chamber itself.

Our goal is to identify errors of the first category, though the first three are convoluted together in a statistical distribution, and the fourth can only be diagnosed by an independent method (such as local alignment techniques described in the previous sections).

Assuming that we can isolate geometric residuals Δx^{geom} , Δy^{geom} , $\Delta \frac{dx}{dz}^{\text{geom}}$, and $\Delta \frac{dy}{dz}^{\text{geom}}$, the alignment corrections δ_x , δ_y , δ_z , δ_{ϕ_x} , δ_{ϕ_y} , and δ_{ϕ_z} can be computed by solving the equation:

$$\begin{pmatrix} \Delta x^{\text{geom}} \\ \Delta y^{\text{geom}} \\ \Delta \frac{dx}{dz}^{\text{geom}} \\ \Delta \frac{dy}{dz}^{\text{geom}} \end{pmatrix} = \begin{pmatrix} 1 & 0 & -\frac{dx}{dz} & -y\frac{dx}{dz} & x\frac{dx}{dz} & -y \\ 0 & 1 & -\frac{dy}{dz} & -y\frac{dy}{dz} & x\frac{dy}{dz} & x \\ 0 & 0 & 0 & -\frac{dx}{dz}\frac{dy}{dz} & 1 + \left(\frac{dx}{dz}\right)^2 & -\frac{dy}{dz} \\ 0 & 0 & 0 & -1 - \left(\frac{dy}{dz}\right)^2 & \frac{dx}{dz}\frac{dy}{dz} & \frac{dx}{dz} \end{pmatrix} \begin{pmatrix} \delta_x \\ \delta_y \\ \delta_z \\ \delta_{\phi_x} \\ \delta_{\phi_y} \\ \delta_{\phi_z} \end{pmatrix}. \quad (22)$$

(The above matrix is an extension of Equation 17 in [9]). For CSCs, the curvilinear residuals $\Delta r\phi^{\text{geom}}$ and $\Delta d(r\phi)/dz^{\text{geom}}$ introduce corrections suppressed by r , the radial distance to the beamline:

$$\begin{pmatrix} \Delta r\phi^{\text{geom}} \\ \Delta \frac{dr\phi}{dz}^{\text{geom}} \end{pmatrix} = \begin{pmatrix} 1 & \left[-\frac{x}{r} + 3\left(\frac{x}{r}\right)^3\right] & -\frac{dx}{dz} & -y\frac{dx}{dz} & x\frac{dx}{dz} & -y \\ 0 & -\frac{dx}{dz}\left(\frac{1}{2r}\right) & 0 & \left[\frac{x}{r} - \frac{dx}{dz}\frac{dy}{dz}\right] & 1 + \left(\frac{dx}{dz}\right)^2 & -\frac{dy}{dz} \end{pmatrix} \begin{pmatrix} \delta_x \\ \delta_y \\ \delta_z \\ \delta_{\phi_x} \\ \delta_{\phi_y} \\ \delta_{\phi_z} \end{pmatrix}. \quad (23)$$

To extract geometric residuals from the measurements, we construct an ansatz describing all effects and fit it to the data. Each of the four observables is represented by a convolution of a Gaussian and a Lorentzian (to model the power-law scattering tails),

$$f(t; t_0, \sigma, \gamma) = \int_{-\infty}^{\infty} \frac{1}{\pi} \frac{\gamma}{(t-s-t_0)^2 + (\gamma)^2} \times \frac{1}{\sqrt{2\pi}\sigma} \exp\left(\frac{-s^2}{2\sigma^2}\right) ds. \quad (24)$$

Position residuals are correlated with their corresponding angle residuals because any error in the propagated track’s direction upstream of the chamber causes errors in its position to grow. Therefore, a 2-D distribution of Δx and $\Delta \frac{dx}{dz}$ is skewed by a parameter $\alpha_{\Delta x}$. A fit function for all

four residuals, F , is the product of four instances of f :

$$\begin{aligned}
 F\left(\Delta x, \Delta y, \Delta \frac{dx}{dz}, \Delta \frac{dy}{dz}; \right. \\
 \left. \Delta x_0, \Delta y_0, \Delta \frac{dx}{dz}_0, \Delta \frac{dy}{dz}_0, \sigma_{\Delta x}, \sigma_{\Delta y}, \sigma_{\Delta \frac{dx}{dz}}, \sigma_{\Delta \frac{dy}{dz}}, \gamma_{\Delta x}, \gamma_{\Delta y}, \gamma_{\Delta \frac{dx}{dz}}, \gamma_{\Delta \frac{dy}{dz}}, \alpha_{\Delta x}, \alpha_{\Delta y}\right) = \\
 f\left(\Delta x; \left(\Delta x_0 + \alpha_{\Delta x} \Delta \frac{dx}{dz}\right), \sigma_{\Delta x}, \gamma_{\Delta x}\right) \times f\left(\Delta \frac{dx}{dz}; \Delta \frac{dx}{dz}_0, \sigma_{\Delta \frac{dx}{dz}}, \gamma_{\Delta \frac{dx}{dz}}\right) \\
 f\left(\Delta y; \left(\Delta y_0 + \alpha_{\Delta y} \Delta \frac{dy}{dz}\right), \sigma_{\Delta y}, \gamma_{\Delta y}\right) \times f\left(\Delta \frac{dy}{dz}; \Delta \frac{dy}{dz}_0, \sigma_{\Delta \frac{dy}{dz}}, \gamma_{\Delta \frac{dy}{dz}}\right) \quad (25)
 \end{aligned}$$

252 The peak of this distribution, $(\Delta x_0, \Delta y_0, \Delta \frac{dx}{dz}_0, \Delta \frac{dy}{dz}_0)$, can be identified as the geometric residu-
 253 als on the left-hand-side of Equation 22 because the observed distribution of residuals is further
 254 convoluted by misalignment. The effect of misalignment is not random; its distribution would
 255 be described by a system of delta distributions that simply replace $(\Delta x_0, \Delta y_0, \Delta \frac{dx}{dz}_0, \Delta \frac{dy}{dz}_0)$ with
 256 $(\Delta x^{\text{geom}}, \Delta y^{\text{geom}}, \Delta \frac{dx}{dz}^{\text{geom}}, \Delta \frac{dy}{dz}^{\text{geom}})$ and introduce a dependence on the track impact positions
 257 x, y and entrance angles $\frac{dx}{dz}, \frac{dy}{dz}$. The final fit function has 16 parameters and 8 dimensions for
 258 DT stations 1–3, 11 parameters and 6 dimensions for CSCs, and 10 parameters, 6 dimensions
 259 for DT station 4 (no access to δ_y). The most relevant projections of an example fit are shown in
 260 Figure 8. The fit is performed by MINUIT [10] with an unbinned maximum likelihood method,
 261 using the weights described above.

262 If the magnetic field or material maps are not perfectly represented in track propagation, resid-
 263 uals will be biased as an antisymmetric function of track curvature, q/p_T . To correct for any
 264 such errors, we split the sample into two bins, one for each charge q , and perform the align-
 265 ment separately in each bin. Muons and antimuons have the same spectral distribution in
 266 cosmic rays (though not the same flux), so a simple average of the $q < 0$ and $q > 0$ results
 267 cancels the antisymmetric bias in all alignment corrections except δ_z . The difference of the two
 268 bins is maximally sensitive to the bias and can be used to measure it.

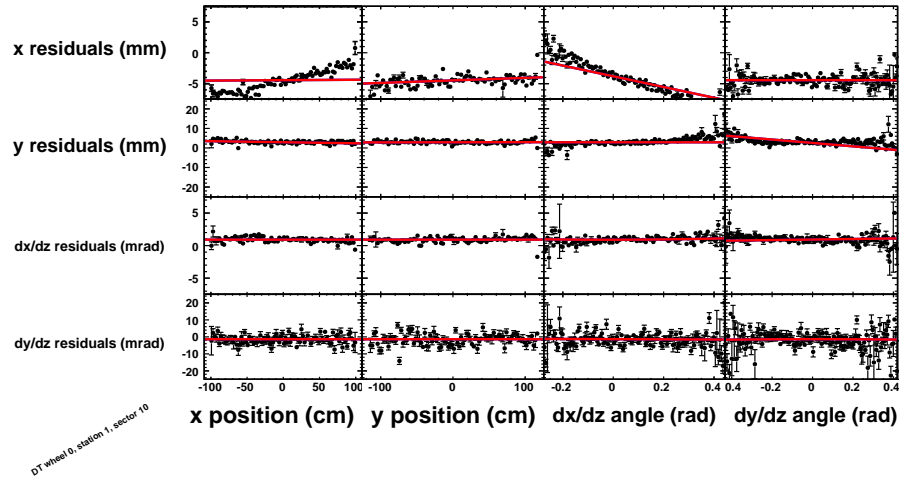
269 Repeated applications of the procedure converge quickly to an optimal solution. Significant
 270 corrections are only observed in the first and second iterations (in data and simulation), so we
 271 always perform three iterations.

272 4.2 The MilliPede Algorithm

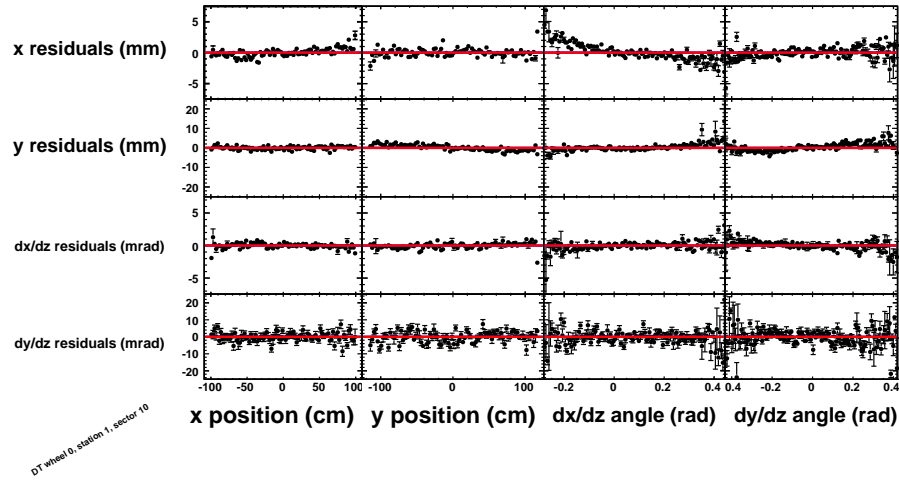
273 The Millepede-based algorithm implemented for global alignment is a particular case of the
 274 most general Millepede algorithm already referred to in section 2. In this case, the ability to fit
 275 tracks and alignment parameters together is parameterized, such that the algorithm can either
 276 let them both float freely (full Millepede), or align chambers to a fixed set of tracks (alignment
 277 to reference).

278 To align chambers in CRAFT, the algorithm was tuned to use a fixed set of tracks from the
 279 tracker. These tracks were propagated into the muon system, and unbiased residuals distribu-
 280 tions were minimized by aligning chambers. In the language of section 2, the matrices $B_j \rightarrow 0$
 281 and $\delta \vec{p}_j$ are no longer parameters in the fit. This also decorrelates alignment parameters in
 282 different chambers, greatly simplifying the alignment.

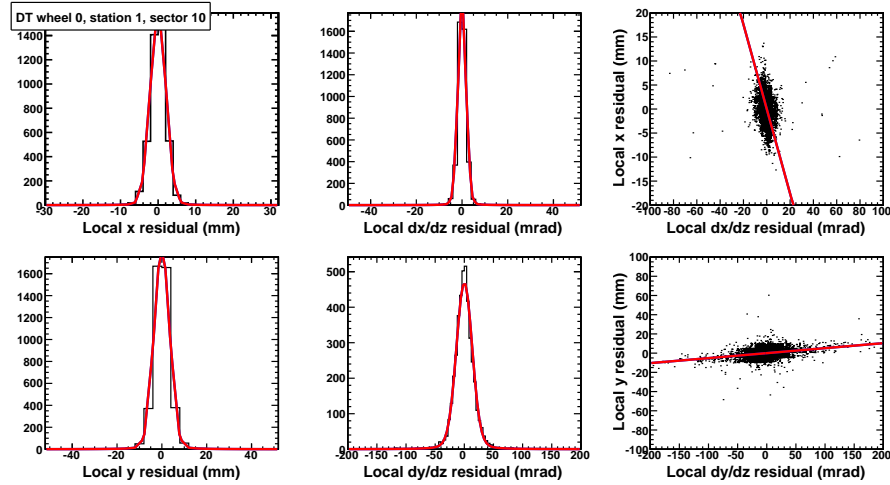
283 As described in section 4.1, the scattering processes that take place in the iron yoke between
 284 chambers deflect muons in a correlated pattern for all the hits in a same chamber. To account



(a) Projection of residuals onto impact point and entrance angle, before alignment.



(b) Projection of residuals onto impact point and entrance angle, after alignment.



(c) Projection of residuals and their correlations, after alignment.

Figure 8: An example fit to cosmic ray data (DT wheel 0, station 1, sector 10) from the HIP algorithm. The red lines are projections of the fit result.

for this correlation, single layer hits and the track intersections associated to them are combined in a linear fit producing four observables for each chamber: the position residuals Δx , Δy and the direction residuals $\Delta \frac{dx}{dz}$ and $\Delta \frac{dy}{dz}$. Just as in the HIP case, these residuals are related to the 6 alignment parameters δ_x , δ_y , δ_z , ϕ_x , ϕ_y and ϕ_z , by Equation 22.

The form of the χ^2 associated with the general Millepede algorithm was shown in Equation 7. In this implementation of the algorithm, χ^2 has the form

$$\chi^2_{\text{track-based}} = \sum_j \left(\Delta \vec{x} - A \cdot \vec{\delta} \right)^T \left(\sigma_{\text{resid}_i}^2 \right)^{-1} \left(\Delta \vec{x} - A \cdot \vec{\delta} \right) \quad (26)$$

where the $\Delta \vec{x}$ is a 4-component vector, and A is the matrix which relates the residuals with the alignment parameters. The $\left(\sigma_{\text{resid}_i}^2 \right)^{-1}$ matrix is the inverse of the covariance calculated from the linear fit estimation of the segments. It includes correlations between positions and directions in both projections.

To avoid the influence of the tails of the residuals distributions, a filtering operation is performed. This is especially important because the tails of the distributions may not be perfectly symmetric. To set cut boundaries for the residuals on each chamber, the peak is fitted to a Lorentz function and residuals are required to be within the full width at half maximum (between $x_0 - \Gamma/2$ and $x_0 + \Gamma/2$ where x_0 and Γ are the peak and full-width at half maximum, respectively). In a one-dimensional application, this alignment fit would correspond to a truncated mean.

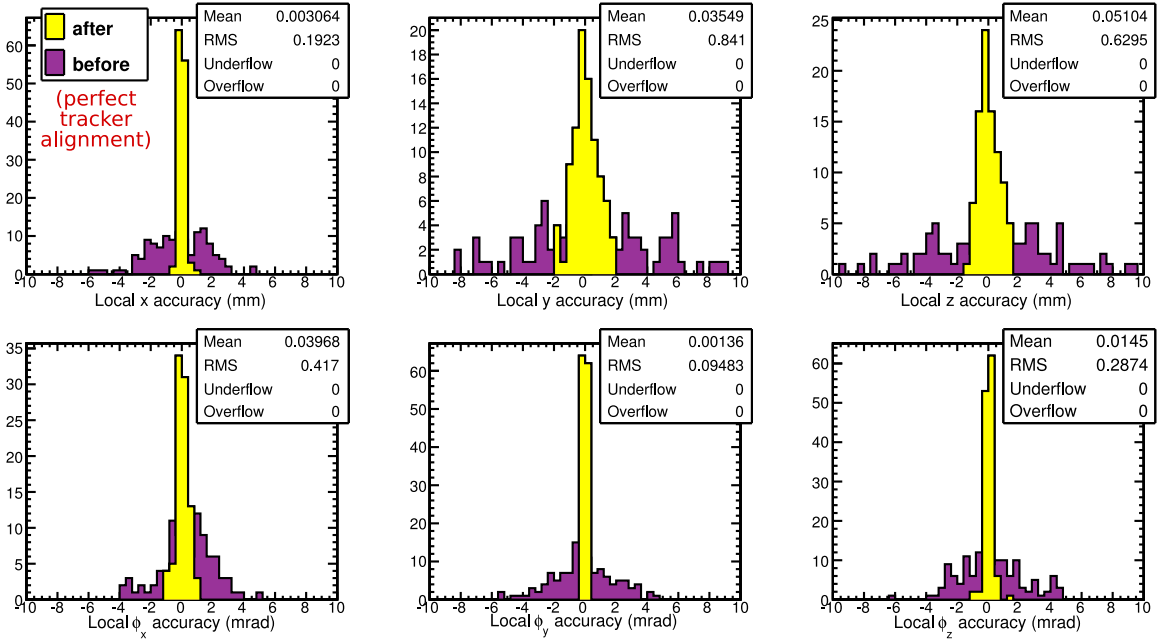
4.3 Monte Carlo Study and Discussion of Systematic Errors

We tested the algorithms with three Monte Carlo simulations: a geometry-only toy simulation to observe the geometric effects independent of detector effects, a full Pythia and GEANT-based $pp \rightarrow \mu + X$ collisions sample, and a full GEANT-based cosmic ray sample. The sizes of the simulated event samples are all large enough for the alignment results to be systematics-limited, and in the GEANT-based simulations, all detector effects were modelled except tracker misalignment, magnetic field errors, and internal muon chamber misalignment. This demonstrates the alignment reach of the algorithms themselves, apart from any possible deficiencies in the input tracks, propagation model, and chamber geometry.

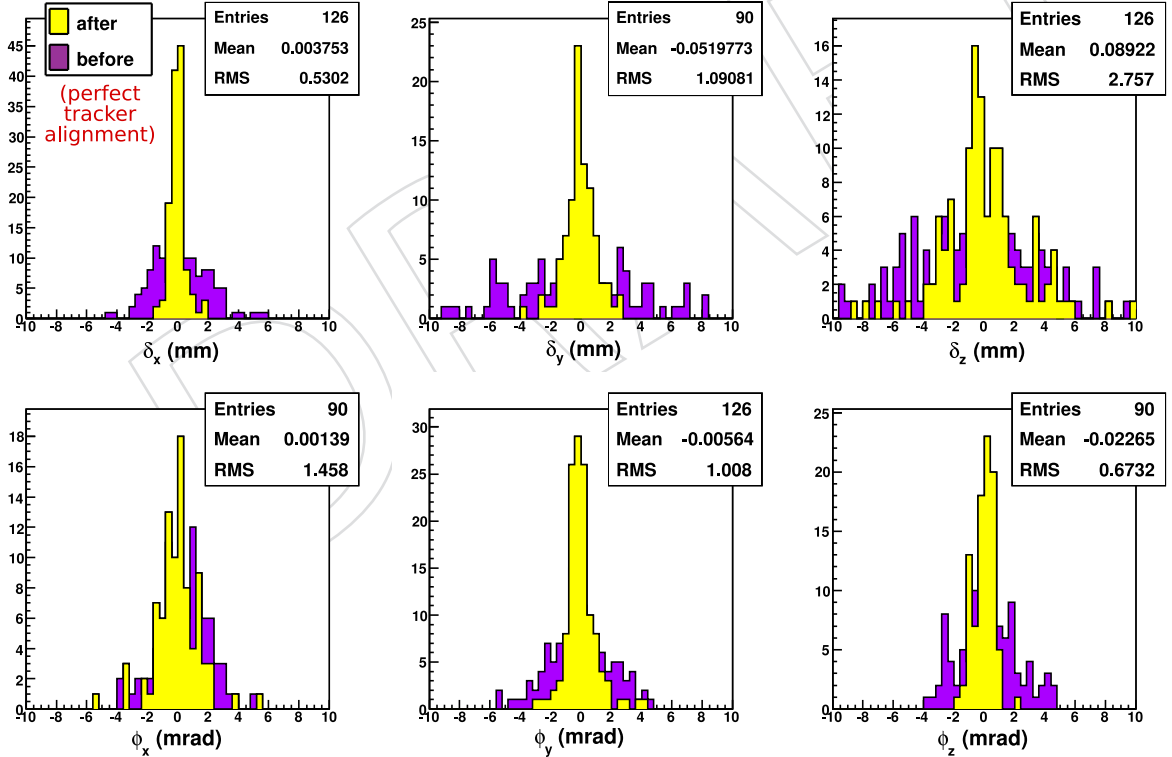
The initial muon system misalignment used in these studies was a Gaussian smearing of chamber positions with a 2 mm standard deviation in δ_x , 4 mm in δ_y and δ_z , and 2 mrad in the three angles. We then applied each procedure to the simulated events in exactly the same way we do to data. Different initial misalignments yield the same results.

Figure 9 shows differences between aligned positions of each parameter and their true positions for the two algorithms in simulated cosmic rays. Interpreting the RMS of these distributions as the alignment accuracy, the δ_x accuracy is 200 μm for HIP, 500 μm for Millepede, close to the intrinsic hit uncertainty of 100–300 μm . Statistical uncertainties returned by the fits are a factor of 3–4 times smaller than the observed accuracy, so this represents the systematic limit of the algorithms as they are currently defined.

There are four classes of systematic error in these procedures: (1) simplifying assumptions about the residuals distributions, (2) biases in the input set of tracks, (3) errors in the propagation of tracks through the muon system, and (4) internal misalignments in the chambers. The exercise described above addresses the first of these, in that the Monte Carlo simulation represents a complete model of the detector response [11], while the alignment algorithms both



(a) HIP aligned-minus-true positions before (purple) and after (yellow) alignment.



(b) Millepede aligned-minus-true positions before (purple) and after (yellow) alignment.

Figure 9: Alignment with simulated cosmic rays using (a) HIP and (b) Millepede. Each entry in the histograms is the difference between the aligned and true values of alignment parameters for one DT chamber. (Only aligned parameters are shown: δ_x , δ_y and δ_z for station 4 and all 6 parameters for stations 1–3.)

include simplifications, optimized for finding the underlying misalignment. The Millepede performance is expected to improve by including a more realistic description of the covariance $\sigma_{\text{resid}_i}^2$ (Equation 26) and a better treatment of the tails of the residuals distribution.

The question of whether input tracks were biased (2) can be addressed in several ways. One is to compare local alignment information with global information, as only the latter would be affected by a biased global tracks. This cross-check was performed and is presented in the next section. Another test uses the fact that muon chambers are large rigid bodies: residuals inside the chambers must be linear with respect to x , y , $\frac{dx}{dz}$, and $\frac{dy}{dz}$, but can be discontinuous at the thresholds between chambers. Discontinuities such as these can only be caused by misalignments, as the input track distribution is unlikely to have features at these points. Small input track biases, below the limit of what could be observed by these methods, would distort the aligned positions of chambers, but in such a way that optimizes the tracking resolution of the selected input tracks.

As tracks propagate into the muon system (3), they may be systematically distorted by potential errors in the magnetic field map and material budget, in a way which reverses sign with muon charge. Application of the procedure described in 4.1 to correct for this effect resulted in negligible alignment differences (100 μm , 200 μm , and 350 μm in δ_x , δ_y , and δ_z and 0.1 mrad in the angles).

Finally, internal misalignments (4) change the effective center of the chamber, making the global alignment results harder to interpret in comparison with physical landmarks (such as the hardware alignment system), but no less valid.

4.4 Global Alignment Results and Cross-Checks

Both the HIP and Millepede algorithms were applied to align a subset of barrel chambers during the CRAFT data-taking run. Wheels -1 , 0 , and $+1$ were aligned, with the exception of sectors 1 and 7 (extreme horizontal sides of the detector) using the barrel section of the tracker as the track reference. The alignment was restricted to this central subset of the barrel chambers because they were the only ones sufficiently illuminated by the primarily vertical distribution of cosmic rays. We also restricted the input to high-quality $100 < p_T < 200$ GeV tracks with at least 15 tracker hits and a tracker reduced $\chi^2 < 10$. Loosening these cuts does not make significantly more chambers available for alignment. The dataset included all runs marked as acceptable for physics in the CMS run registry, with a magnetic field of 3.8 T. The CRAFT period included several on-off cycles of the magnetic field, which were shown to result in reproducible alignments with the hardware system [2] and tracks (within statistical precision).

In addition to the chambers explicitly excluded from alignment due to poor statistics, two chambers next to sectors 1 and 7 (in wheel, station, sector $(-1, 2, 8)$ and $(+1, 3, 8)$) had no tracks passing the cuts and two more $((-1, 1, 12)$ and $(+1, 2, 2))$ failed to converge in HIP, owing to the extreme azimuthal asymmetry of cosmic rays.

We checked our alignment results in four ways: we verified (1) that the algorithms optimized their intended expressions, (2) that they agree with one another, (3) that the new global chamber positions yield the same or better agreement with local measurements, and (4) that the new alignment yields better momentum resolution for tracks.

The simplest way to test the internal consistency of the algorithm (1) is to run the alignment algorithm a second time on the same dataset and verify that the second alignment corrections are always zero. As a sanity check, we also verified that the raw residuals distributions are centered at zero with very high precision. An example of this was shown in Figure 8.

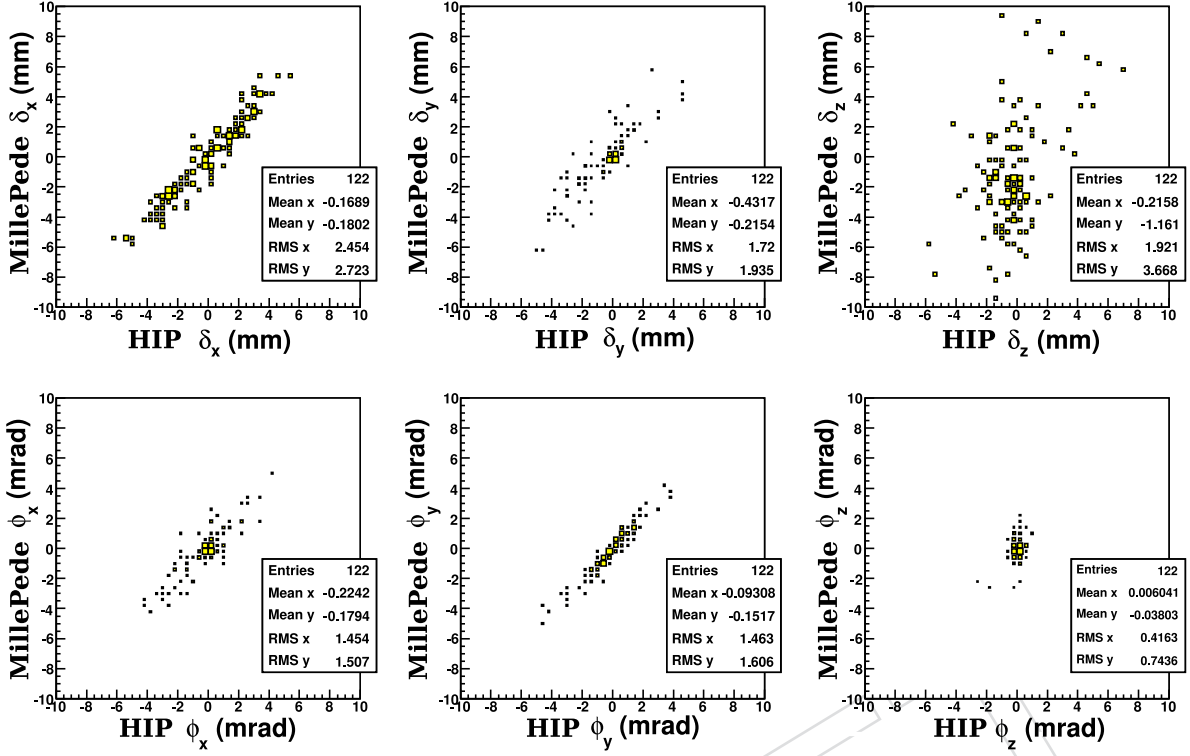
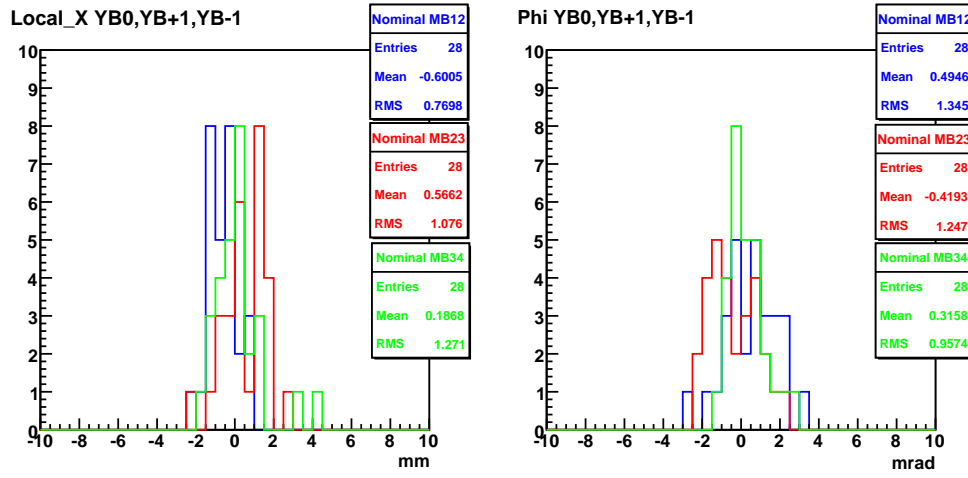


Figure 10: Alignment corrections determined by the HIP and Millepede algorithms. (Only aligned chambers are shown.)

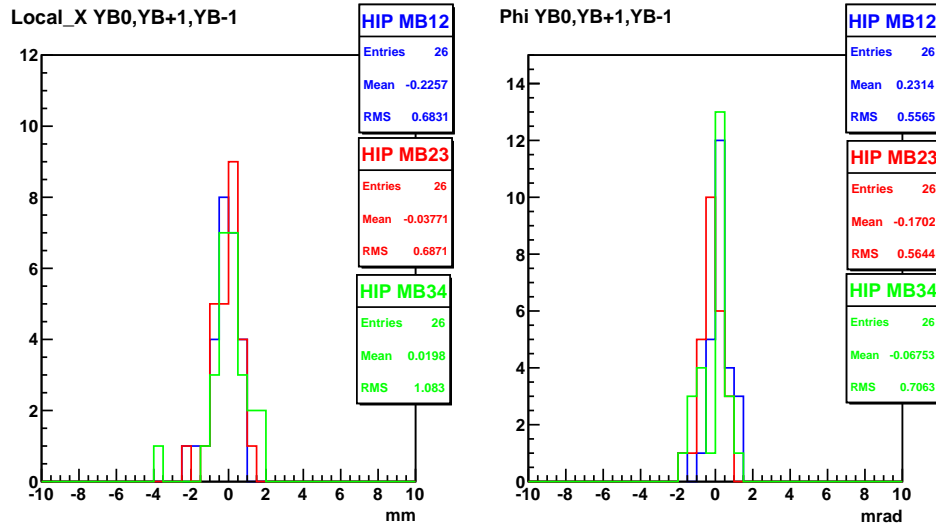
To demonstrate that the two algorithms agree with each other (2), we present corrections computed by each algorithm in a scatter plot 10. Though the corrections were on the order of 0.5–3 mm/mrad, the two algorithms agree with each other within expectations from the Monte Carlo study (Figure 9). The two parameters in which no correlation is observed between the algorithms are δ_z and δ_{ϕ_z} , which are the most likely to be affected by the treatment of tails in residuals distributions. The distributions of δ_y and δ_{ϕ_x} have sharp peaks at zero: these parameters cannot be aligned in station 4, because station 4 chambers do not measure Δy residuals.

Local alignment measurements to test consistency between global data and local data (3) were derived by extrapolating linear track segments from one chamber to the next (in the same sector, neighboring stations). This verification procedure introduces information not used in the alignment itself, namely the higher precision with which tracks can be propagated over a short distance (1 meter) than a long distance (3–6 meters).

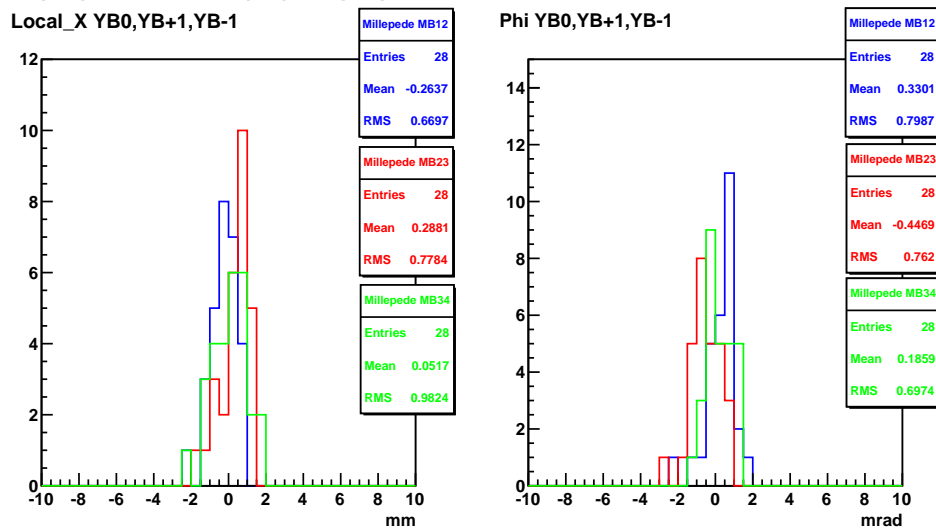
For this diagnostic, tracks were selected with $p_T > 50$ GeV and a correction was applied to cancel the effect of the magnetic field by taking advantage of the fact that positively- and negatively-charged tracks are pushed in opposite directions. To compare the initial state with the results of each algorithm in all station-pairs, sectors, and wheels, we filled histograms with the fitted Gaussian peak of each comparison, shown in Figure 11. Though the global algorithms changed the positions of chambers by 2.5 mm in δ_x and 1.5 mrad in δ_{ϕ_y} (RMS in Figure 10), local differences of 0.8–1.3 mm and 1.0–1.3 mrad are not only maintained but reduced by 10% to a factor of 2. As expected, the chambers which are closest to the tracker (station 1-to-2 differences) are the most precisely aligned. The individual outliers in station 4 contain internal structure in their residuals distributions which are the subject of further study.



(a) Before global alignment



(b) Results from the HIP algorithm



(c) Results from the Millepede algorithm

Figure 11: Local differences in alignment as measured by segments. Each histogram entry is a pair of chambers in neighboring stations, but the same wheel and sector. The three histograms show station 1-to-2 differences (blue), 2-to-3 differences (red), and 3-to-4 differences (green).

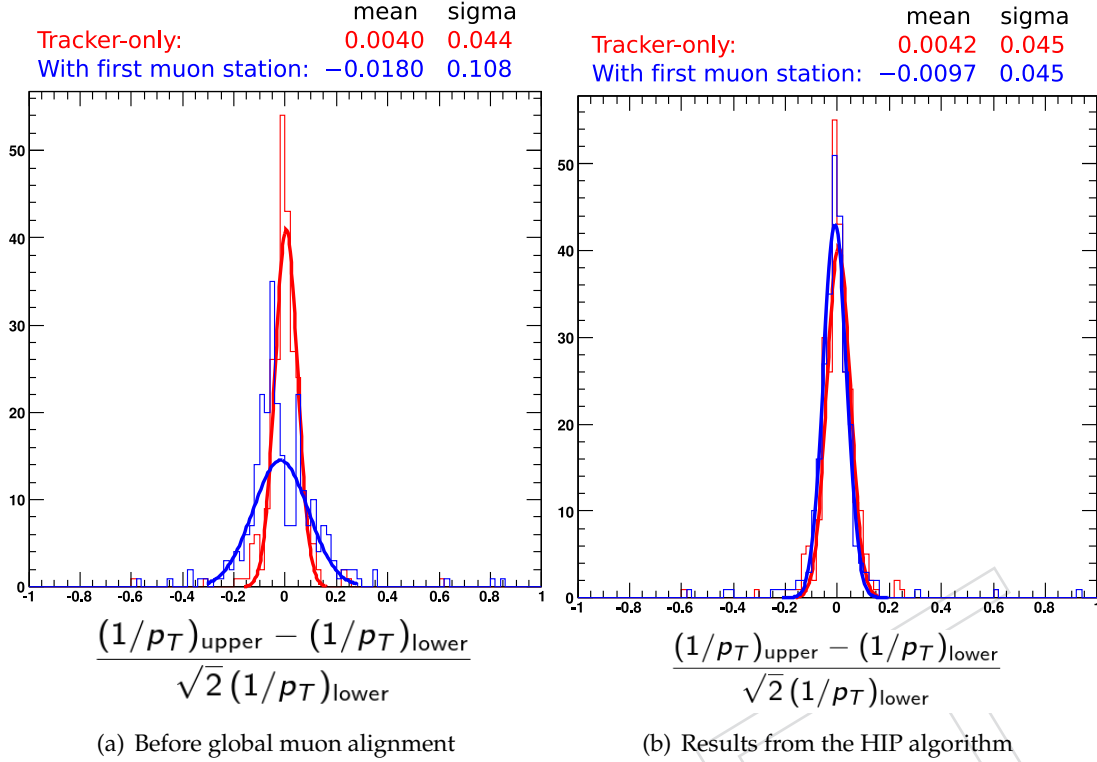


Figure 12: Top vs. bottom $1/p_T$ comparison for $p_T \gtrsim 200$ GeV split cosmic rays.

To verify that the new alignment (in this case, HIP only) improves momentum resolution (4), we selected cosmic rays with $p_T > 200$ GeV, split each into two tracks near the origin (similar to what would be observed in LHC collisions), and compared the momentum of the top and bottom fits. Since the cosmic ray muon is a single particle, any mismatch between the halves is purely instrumental. Cosmic rays have a steeply falling distribution, so most of the selected tracks have p_T close to 200 GeV. The alignment was performed using tracks with $100 < p_T < 200$ GeV tracks, so the diagnostic sample is statistically independent from the alignment. Figure 12 compares tracker-only tracks and tracks reconstructed with muon hits (first muon station only), before and after the global muon alignment.

5 Conclusions

In this note, we have demonstrated a variety of software procedures for aligning different parts of the muon system: layers in DT chambers, CSC chambers in rings, and global positions of DT chambers relative to the central tracker, using charged tracks. We have fully exploited the available data, horizontal LHC beam-halo muons and vertical cosmic rays.

These procedures will be used without major modifications to re-align the muon system with muons from LHC collisions, once such data are available. The azimuthally-symmetric and broad pseudorapidity distribution of collisions muons will allow us to extend the global alignment to all muon chambers. Although the endcap chambers are sensitive to only three parameters, $\delta_{r\phi}$, δ_{ϕ_y} and δ_{ϕ_z} (the same as local CSC alignment), these parameters can be determined with $400 \mu\text{m}$, 0.4 mrad , and 0.6 mrad resolution with similar results for all degrees of freedom in the muon barrel, according to 50 pb^{-1} simulations. To constrain the remaining CSC parameters, we can exploit the complementarity of the endcap hardware alignment system [2] (which measure δ_z and δ_{ϕ_x} directly), and independently test its validity in $\delta_{r\phi}$.

Moreover, the addition of collisions muons and larger beam-halo datasets will allow new cross-checks to be performed, as the local CSC alignment (section 3) and CSC layer alignment can be performed with both collisions and beam-halo, so we can doubly cross-check by performing the same method with different track sources and different methods with the same track source. Similarly, collisions and cosmic rays can both be used in the barrel, and they differ in how the reference tracks sample the tracker, and hence potential input track bias.

By verifying the muon alignment in as many ways as possible, we can add confidence to the muon momentum resolution at all energy scales, improving sensitivity to signatures of new physics.

References

- [1] CMS Collaboration, R. A. et al., “The CMS experiment at the CERN LHC,” *JINST* **0803** (2008) S08004. JINST,0803,S08004. doi:10.1088/1748-0221/3/08/S08004.
- [2] CMS Collaboration, CFT-09-017, “Aligning the CMS Muon Chambers with the Hardware Alignment System during the CRAFT08 Exercise,” *J. Inst.* (2009).
- [3] CMS Collaboration, CFT-09-007, “CRAFT Workflows Paper: from Detector to Analysis,” *J. Inst.* (2009).
- [4] CMS Collaboration, CFT-09-003, “Alignment of the CMS inner tracking system with cosmic ray particles,” *J. Inst.* (2009).
- [5] CMS Collaboration, M. Grünwald, “CMS Conventions.” <https://twiki.cern.ch/twiki/bin/view/CMS/CMSConventions>.
- [6] V. Blobel, “Software alignment for tracking detectors,” *Nucl. Instrum. Meth.* **A566** (2006) 5–13. NUIMA,A566,5. doi:10.1016/j.nima.2006.05.157.
- [7] CMS Collaboration, S. M. et al., “Drift Tubes Quality Assurance and Quality Control.” <http://cms.pd.infn.it/edr2/qcdoc.pdf>.
- [8] CMS Collaboration, G. B. et al., “DT Chamber Calibration web database.” <http://kismalac.phys.klte.hu/cgi-bin/Survey/indexpage.pl>.
- [9] V. Karimaki, A. Heikkinen, T. Lampen, and T. Linden, “Sensor alignment by tracks,” arXiv:physics/0306034. PHYSICS/0306034.
- [10] F. James and M. Roos, “Minuit: A System for Function Minimization and Analysis of the Parameter Errors and Correlations,” *Comput. Phys. Commun.* **10** (1975) 343–367. CPHCB,10,343. doi:10.1016/0010-4655(75)90039-9.
- [11] CMS Collaboration, CFT-09-012, “Results on Local Muon Reconstruction in DT chambers from analysis of CRAFT data,” *J. Inst.* (2009).